The Astrophysical Journal, 754:55 (13pp), 2012 July 20 doi:10.1088/0004-637X/754/1/55

INFLUENCE OF THE POLAR CAP CURRENT ON PULSAR POLARIZATION

D. Kumar and R. T. Gangadhara
Indian Institute of Astrophysics, Bangalore 560 0034, India; dinesh@iiap.res.in, ganga@iiap.res.in
Received 2012 February 8; accepted 2012 May 18; published 2012 July 5

ABSTRACT

We have developed a model for the polarization of curvature radiation by taking into account the polar-cap-current-induced perturbation on the dipolar magnetic field. We present the effects of the polar cap current on the pulsar radio emission in an artificial case when the rotation effects, such as aberration and retardation, are absent. Our model indicates that the intensity components and the polarization angle inflection point can be shifted to either the leading or the trailing side depending upon the prevailing conditions in the viewing geometry, the non-uniformity in source distribution (modulation), and the polar-cap-current-induced perturbation. Also, we find evidence for the origin of symmetric-type circular polarization in addition to the antisymmetric type. Our model predicts a stronger trailing component compared to that on the leading side of a given cone under some specific conditions.

Key words: polarization – pulsars: general – radiation mechanisms: non-thermal

1. INTRODUCTION

Pulsars are universally accepted as fast rotating neutron stars with a very strong magnetic field ($\sim 10^8$–10^{12} G), which is predominantly dipolar. Their radio emission is thought to be curvature emission from relativistic plasma streaming out along the open field lines of a dipole whose foot points on the neutron star surface define the polar cap (Sturrock 1971; Ruderman & Sutherland 1975; Cheng & Ruderman 1980). The simplistic picture of pulsar radio emission that we can gather from the polar cap emission models is as follows. The rotationally induced, very strong electric field component parallel to the magnetic field pulls out the primary plasma from the neutron star surface and accelerates it to very high energies with a Lorentz factor of $\gamma \sim 10^5$–10^7. These ultrarelativistic primary particles emit γ-ray photons through curvature and synchrotron radiations, which in turn produce the secondary electron–positron (e^-, e^+) pair plasma by their interaction with a strong magnetic field. The secondary plasma further undergoes the pair cascade process and develops into a high-density plasma of $\gamma \sim 10^2$–10^3. Once the density of the pair plasma becomes comparable to the Goldreich–Julian charge density, it shields the parallel electric field component (Goldreich & Julian 1969). Hence, the plasma motion becomes "force free" along the field lines and emits curvature radiation due to the curvature of the field lines. Since the brightness temperature of the pulsar radio emission is very high ($\sim 10^{25}$–10^{30} K), the emission is believed to be coherent emission from plasma.

Pulsars show a high degree of linear polarization with a systematic "S"-shaped polarization position angle (PPA) swing, which is a characteristic property of pulsar signals. The "rotating-vector-model" (RVM) of Radhakrishnan & Cooke (1969) attributes this characteristic "S" curve to an underlying geometry, wherein the magnetic field is assumed to be mainly dipolar, and relativistic beaming is in the direction of field line tangents. Ever since the success of RVM, the fitting of pulsar polarization angle profiles to the model has been attempted to constrain the underlying emission geometry, such as the magnetic axis inclination angle with respect to the rotation axis and the sight line impact angle with respect to the magnetic axis. However, some pulsars show that the polarization angle behavior deviates from the standard "S" curve, particularly in millisecond pulsars, where the polarization sweep is noisy and flatter on average (Xilouris et al. 1998). Several relativistic and plasma effects have been proposed to understand these deviations: plasma propagation effects (Barnard & Arons 1986; McKinnon 1997), aberration of the beaming direction from strict parallelism (Blaskiewicz et al. 1991; Dyks 2008; Kumar & Gangadhara 2012), distortion of the underlying dipole field due to the field-aligned polar cap current (PC-current; Hibschman & Arons 2001), or multiple interacting orthogonal polarization modes (McKinnon & Stinebring 1998).

Phenomenologically, pulsar emission is recognized as a central "core" arising from a region near the magnetic pole and surrounding "cones" from concentric rings around the pole (e.g., Rankin 1983, 1990, 1993; Mitra & Deshpande 1999; Gangadhara & Gupta 2001; Mitra & Rankin 2002). However, due to an asymmetry in the phase location of the components, there are some contrary arguments that the emission is "patchy" (Lyne & Manchester 1988). Pulsars also show an asymmetry in the strength of component intensity between the leading and trailing sides. The asymmetry observed both in the strength and the phase location of the components has been attributed to the effects of rotation such as aberration and retardation (e.g., Blaskiewicz et al. 1991; Gangadhara & Gupta 2001; Gupta & Gangadhara 2003; Dyks et al. 2004; Thomas & Gangadhara 2007; Dyks 2008; Dyks et al. 2010; Thomas et al. 2010; Kumar & Gangadhara 2012). Due to the rotationally induced aberration and asymmetry in the curvature of the source trajectory, the inflection point of the PPA profile lags the peak of the central intensity component (core; Blaskiewicz et al. 1991; Thomas & Gangadhara 2010; Dyks 2008; Kumar & Gangadhara 2012), and the leading side components become stronger and broader than the corresponding ones on the trailing side (Thomas & Gangadhara 2007; Dyks et al. 2010; Thomas et al. 2010; Kumar & Gangadhara 2012).

In general, circular polarization is common in pulsar emission, but diverse in nature (Han et al. 1998; You & Han 2006). The research related to its origin is still of great importance from the point of view of the emission mechanism. There are two types of models for the origin of the circular polarization: intrinsic to the emission mechanism (e.g., Michel 1987; Gil & Snakowski 1990a, 1990b; Radhakrishnan & Rankin 1990; Gangadhara 1997, 2010; Kumar & Gangadhara 2012) and

generated by the propagation effects (e.g., Cheng & Ruderman 1979; Melrose 2003). Only the "antisymmetric"-type circular polarization was thought to be an intrinsic property of curvature radiation. Very recently, Kumar & Gangadhara (2012) have shown that the "symmetric"-type circular polarization (where the circular sign remains the same throughout a component or pulse) is also possible within the framework of curvature radiation, which takes into account the pulsar rotation and modulation (nonuniform plasma distribution). They have made an attempt to simulate the diverse behavior of polarization properties of pulsar radio emission by developing a relativistic model on full polarization of curvature radiation.

Since the polarization behavior of pulsars is believed to depend upon the underlying geometry of the emission region, any perturbation to the dipole field is expected to be reflected in the polarization profiles. The induced toroidal magnetic field due to field-aligned poloidal currents above the polar cap perturbs the dipole field and it is quite significant in affecting the PPA (Hibschman & Arons 2001) and introduces a phase shift into the intensity components (Gangadhara 2005). It is shown that the PC-current can only introduce an offset into the PPA swing, but there is no significant phase shift into the inflection point. The full polarization model that describes all the polarization parameters of radio emission in the PC-current perturbed dipole magnetic field does not exist. So, in an attempt to understand the PC-current-induced perturbation on the pulsar radio emission and polarization, we develop a complete polarization model by taking into account only the PC-currents. We derive the viewing geometry for the perturbed dipole field in Section 2. In Section 3, we present the simulation of typical polarization profiles for the cases of uniform and nonuniform distributions of radiation sources. In Section 4 we provide the discussion, and in Section 5 the conclusion.

2. PERTURBATION OF THE MAGNETIC FIELD AND EMISSION GEOMETRY

In spherical polar coordinates (r, θ, ϕ) centered on the magnetic axis, the unperturbed dipole field is given as

$$\boldsymbol{B_0} = \left(\frac{2\mu\cos\theta}{r^3}, \frac{\mu\sin\theta}{r^3}, 0\right), \tag{1}$$

where μ is the magnetic moment, θ is the magnetic colatitude, and r is the radial distance from the origin. Most of the polar cap models of pulsar emission include a current of relativistic charged particles streaming out along the open field lines, which is approximately equal to the Goldreich–Julian charge density ($J_{\rm GJ}$),

$$\boldsymbol{J} = -\frac{1}{2\pi}\varsigma(\boldsymbol{\Omega}\cdot\boldsymbol{B_0})\hat{B}_0, \tag{2}$$

where $\varsigma = J/J_{\rm GJ}$ is a scale factor of order unity, reflecting our ignorance of the actual current, and $\boldsymbol{\Omega}$ is the pulsar angular velocity. For simplicity, we treat ς to be a constant quantity throughout this work.

By assuming a small polar cap so that the variation in $\boldsymbol{\Omega}\cdot\boldsymbol{B_0}$ across the polar cap is also small, and that $\boldsymbol{B_0}$ is a point dipole with an axisymmetric current flow, the induced magnetic field due to the field-aligned current is given as (Hibschman & Arons 2001)

$$\boldsymbol{B_1} = \left(0, 0, -\frac{2\mu\sin\theta}{r^3}\varsigma\frac{r}{r_{\rm LC}}\cos\alpha\right), \tag{3}$$

which is purely toroidal and axisymmetric with respect to the magnetic axis, i.e., independent of the magnetic azimuth ϕ. The angle α is the magnetic axis inclination angle, and $r_{\rm LC} = c/\Omega = cP/(2\pi)$ is the light cylinder radius, where c is the speed of light and P is the pulsar rotation period. Then the perturbed dipole field $\boldsymbol{B} = \boldsymbol{B_0} + \boldsymbol{B_1}$ with $B_1 \ll B_0$ is also axisymmetric with respect to the magnetic axis.

The differential equations for the magnetic field lines are

$$\frac{dr}{B_r} = \frac{rd\theta}{B_\theta} = \frac{r\sin\theta d\phi}{B_\phi}, \tag{4}$$

where B_r, B_θ, and B_ϕ are the respective r, θ, and ϕ components of $\boldsymbol{B}$ in polar coordinates. Substituting the expressions for B_r, B_θ, and B_ϕ into Equation (4) yields the following three differential equations for the magnetic field lines:

$$\frac{1}{r}dr = 2\cot\theta d\theta, \tag{5}$$

$$\frac{r}{\sin\theta}d\theta = -\frac{r_{\rm LC}}{2\varsigma\cos\alpha}d\phi, \tag{6}$$

and

$$\frac{1}{\cos\theta}dr = -\frac{r_{\rm LC}}{\varsigma\cos\alpha}d\phi. \tag{7}$$

Since Equation (7) can be deduced from Equations (5) and (6), magnetic field lines can be defined uniquely by the earlier two equations.

Integration of Equation (5) gives

$$r = K_1\sin^2\theta, \tag{8}$$

where K_1 is the integration constant. Using $r = r_{\rm max} = r_e$, the field line constant at $\theta = \pi/2$, we obtain $K_1 = r_e$. Then Equation (8) becomes

$$r = r_e\sin^2\theta. \tag{9}$$

Substitution of Equation (9) into Equation (6) and integration gives

$$r_e\cos\theta = \frac{r_{\rm LC}}{2\varsigma\cos\alpha}\phi + K_2, \tag{10}$$

where K_2 is the integration constant. Using $\phi = \phi_i$ at $\theta = \theta_i$, we obtain $K_2 = r_e\cos\theta_i - r_{\rm LC}\phi_i/(2\varsigma\cos\alpha)$, where θ_i and ϕ_i are the initial colatitude and azimuth, respectively. By substituting K_2 into Equation (10) we get

$$\phi = \phi_i + \frac{2r_e}{r_{\rm LC}}\varsigma\cos\alpha(\cos\theta - \cos\theta_i). \tag{11}$$

The position vector $\boldsymbol{r}$ of an arbitrary point P_e on a perturbed dipolar field line is given by Equation (1) of Gangadhara (2010), where the parameter ϕ has to be replaced by the expression that we have given in Equation (11). By using $\alpha = 30^\circ$, rotation phase $\phi' = 30^\circ$, $r_e = r_{\rm LC}$, $P = 1$ s, $\varsigma = 1$, $\theta_i = 0^\circ$, ϕ_i from 0° to 360° in steps of 45°, and r from 0 to $0.6r_{\rm LC}$ we have traced the field lines and presented them in Figure 1. Dashed line curves represent the field lines of an actual dipole while the solid line curves represent those of the perturbed dipole. PC-currents induce the toroidal component of the magnetic field, and hence there is an azimuthal twist in the field lines of the perturbed field with respect to the magnetic axis.

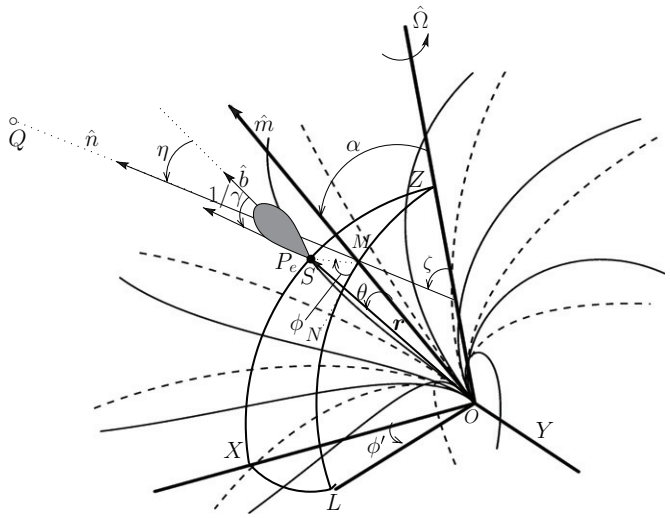

Figure 1. Geometry for curvature radiation from a relativistic source S in a distorted (or perturbed) magnetic dipole due to polar cap currents. Magnetic axis $\hat{m}$ is inclined with respect to pulsar rotation axis $\hat{\Omega}$ by an angle α. The dashed line curves represent the field lines of a pure dipole whereas the solid line curves represent those of a perturbed dipole. The observer's sight line $\hat{n}$ lies in the fiducial plane (XZ-plane), and the observation point Q is at a distance R from the emission point P_e. We have used $\alpha = 30^\circ$, $\phi' = 30^\circ$, $r_e = 1r_{\rm LC}$, $P = 1$ s, $\varsigma = 1$, ϕ_i from 0° to 360° in steps of 45°, $\theta_i = 0^\circ$, and r from 0 to $0.6r_{\rm LC}$ to sketch the field lines of the pure dipole and those of the perturbed dipole.

The curvature of the perturbed dipolar field line is given by

$$\boldsymbol{k} = \frac{d\hat{\boldsymbol{b}}}{ds} = \frac{1}{|\mathbf{b}|}\frac{d\hat{\boldsymbol{b}}}{d\theta}, \tag{12}$$

where $ds = |\mathbf{b}|d\theta$ is the arc length of the field line, $\hat{\boldsymbol{b}} = \boldsymbol{b}/|\boldsymbol{b}|$, and $\boldsymbol{b} = d\boldsymbol{r}/d\theta$ is the field line tangent. The magnitude of $\boldsymbol{b}$ can readily be found to be

$$|\boldsymbol{b}| = \frac{r_e \sin\theta}{2}\sqrt{10 + 6\cos 2\theta + 4\Delta^2 \sin^2\theta}, \tag{13}$$

where the parameter $\Delta = 2\varsigma r \cos\alpha / r_{\rm LC}$. Then, the radius of the curvature $\rho = 1/|\boldsymbol{k}|$ of a field line becomes

$$\rho = \frac{r_e \sin\theta d_1^2}{2\sqrt{2}\sqrt{D_1 + D_2\cos 2\theta - D_3 \sin 2\theta}}, \tag{14}$$

where $\boldsymbol{k} = d\hat{\boldsymbol{b}}/ds$ is the curvature vector of the field line,

$$\begin{aligned} D_1 &= 2(9 + 18\Delta^2 + \Delta^4)d_1^2 + (5 + \Delta^2)d_2^2, \\ D_2 &= 24\Delta^2 d_1^2 + (3 - \Delta^2)d_2^2, \\ D_3 &= 6(1 - \Delta^2)d_1 d_2, \end{aligned}$$

and

$$\begin{aligned} d_1 &= 10 + 6\cos 2\theta + 4\Delta^2 \sin^2\theta, \\ d_2 &= 6(1 - \Delta^2)\sin 2\theta. \end{aligned}$$

The velocity of the relativistic source (particle or plasma bunch), which is constrained to move along the perturbed field line, is given by

$$\boldsymbol{v} = \kappa c \hat{\boldsymbol{b}}, \tag{15}$$

where the parameter $\kappa = \sqrt{1 - 1/\gamma^2}$ with γ being the source Lorentz factor. Then the acceleration $\boldsymbol{a} = d\boldsymbol{v}/dt$ due to the curvature of field lines is given by

$$\boldsymbol{a} = (\kappa c)^2 \boldsymbol{k}, \tag{16}$$

where we have used $ds = |\mathbf{b}|d\theta = \kappa c dt$.

The accelerating relativistic particles emit beamed emissions in the direction of their velocities. At any given rotation phase ϕ' and emission altitude r, the observer receives the emissions from a finite beaming region consisting of the flux of magnetic field lines. The observer receives a maximum beamed emission when sight line $\hat{n}$ exactly aligns with the source velocity $\boldsymbol{v}$. Observer sight line $\hat{n} = (\sin\zeta, 0, \cos\zeta)$, where the angle $\zeta = \alpha + \sigma$ with σ being the sight line impact angle with respect to the magnetic axis. Since the beaming angle of the beamed emission from a relativistic particle is $\sim 1/\gamma$ about its velocity, the beaming region boundary can be specified by the emission points at which $\hat{n} \cdot \hat{b} = \cos(1/\gamma)$. Therefore the emission points within the beaming region satisfy the condition $-1/\gamma \leqslant \eta \leqslant 1/\gamma$, where η is the angle between $\hat{n}$ and $\hat{b}$. Following Kumar & Gangadhara (2012), we define the emission point coordinates: magnetic colatitude and azimuth of the emission points within the beaming region as θ_e and ϕ_e, respectively, wherein at the center of the beaming region $\theta_e = \theta_0$ and $\phi_e = \phi_0$.

Next, for a given emission altitude r, we find the emission point coordinates (θ_0, ϕ_0) and the range of θ and ϕ, which define the beaming region boundary. Solving $\hat{m} \cdot \hat{b} = \cos\tau = (1 + 3\cos 2\theta)/\sqrt{10 + 6\cos 2\theta + 4\Delta^2 \sin^2\theta}$ for θ gives

$$\cos 2\theta = \frac{1}{3}\left(\left(1 - \frac{\Delta^2}{3}\right)\cos^2\tau + \cos\tau\sqrt{\left(1 - \frac{\Delta^2}{3}\right)^2 \cos^2\tau + 8\left(1 + \frac{\Delta^2}{3}\right)} - 1\right), \tag{17}$$

where τ is the angle between $\hat{m}$ and $\hat{b}$. But the angle Γ between $\hat{m}$ and $\hat{n}$ is given by

$$\cos\Gamma = \cos\alpha\cos\zeta + \sin\alpha\sin\zeta\cos\phi'.$$

For an exact alignment of $\hat{n}$ and $\hat{b}$ at the beaming region center, $\hat{n} \cdot \hat{b} = 1$, which implies $\tau = \Gamma$. Hence we have

$$\cos 2\theta_0 = \frac{1}{3}\left(\left(1 - \frac{\Delta^2}{3}\right)\cos^2\Gamma + \cos\Gamma\sqrt{\left(1 - \frac{\Delta^2}{3}\right)^2 \cos^2\Gamma + 8\left(1 + \frac{\Delta^2}{3}\right)} - 1\right). \tag{18}$$

Next, by solving $\hat{n} \times \hat{b} = 0$, we obtain

$$\sin\phi_0 = \frac{\csc\Gamma(\sin\zeta(\Delta\cos\alpha\cos\phi' - 3\cos\theta\sin\phi') - \Delta\sin\alpha\cos\zeta)}{\sqrt{\Delta^2 + 9\cos^2\theta}} \tag{19}$$

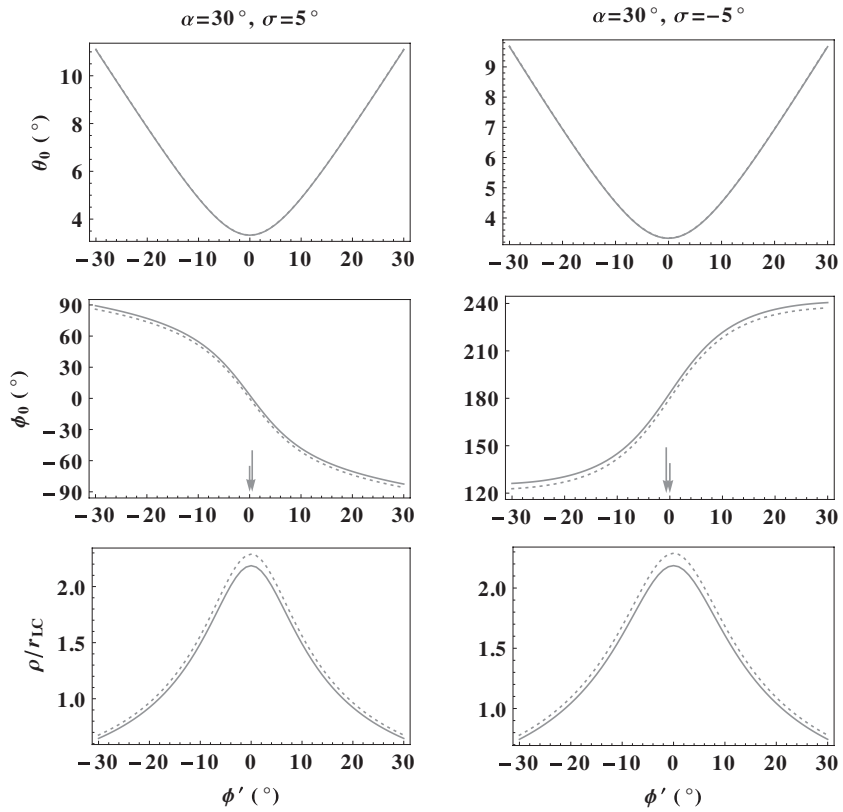

Figure 2. Magnetic colatitude θ_0 and azimuth ϕ_0 of the beaming region center are plotted as functions of rotation phase ϕ'. The radius of curvature ρ is plotted in the lower panels. The dotted and solid line curves are for the unperturbed and perturbed cases of the dipolar magnetic field. The parameters used are $r_n = r/r_{\rm LC} = 0.1$, $P = 1$ s, and $\varsigma = 1$. In the ϕ_0 panels, the long and short arrows indicate the antisymmetric and inflection points of ϕ_0 in the perturbed dipole, respectively.

and

$$\cos\phi_0 = \frac{\csc\Gamma(\sin\zeta(3\cos\alpha\cos\theta\cos\phi' + \Delta\sin\phi') - 3\sin\alpha\cos\zeta\cos\theta)}{\sqrt{\Delta^2 + 9\cos^2\theta}}. \quad (20)$$

In Figure 2 we have plotted the emission coordinates (θ_0, ϕ_0) of the beaming region center and the corresponding radius of curvature ρ of the source trajectory at those points as functions of the rotation phase. We chose the parameters $\alpha = 30^\circ$, $\sigma = \pm 5^\circ$, the emission altitude $r_n = r/r_{\rm LC} = 0.1$, $P = 1$ s, and $\varsigma = 1$. The dotted line curves are for the parameters in the case of an unperturbed dipole, and the solid line curves represent those in the perturbed case. The colatitude θ_0 is found to remain unaffected, whereas there is an upward vertical shift in azimuth ϕ_0 due to the induced toroidal magnetic field. Therefore at any rotation phase, the radiation is aberrated in the direction opposite to the direction of the pulsar rotation for positive σ (i.e., for $\zeta > \alpha$), whereas for negative σ (i.e., for $\zeta < \alpha$) it is aberrated in the direction of the pulsar rotation. In other words, emission locations in ϕ get shifted to later phases with respect to those due to the unperturbed dipole for positive σ, whereas for negative σ they get shifted to earlier phases (the phase shift of an antisymmetric point of ϕ_0 with respect to $\phi' = 0$ is indicated by the longer arrows). Note that the inflection point of ϕ_0 (the phase at which the ϕ_0 curve has a maximum slope) is found to remain unaffected as indicated by the shorter arrows. Since the effect of the induced toroidal component of the magnetic field due to PC-currents is just a twist of the field lines around the magnetic axis and is the same on both the leading and trailing sides, ρ in the perturbed configuration will remain almost symmetric with respect to the phase $\phi' = 0^\circ$, similar to that in the unperturbed one but with smaller values because of an induced curvature.

Next at $\phi = \phi_0$, we solve $\hat{n}\cdot\hat{b} = \cos\eta_{\rm max} = \cos(1/\gamma)$ and find the allowed range of τ: $\Gamma - 1/\gamma \leqslant \tau \leqslant \Gamma + 1/\gamma$, and hence deduce the allowed range of θ from Equation (17). Then for any θ within its allowed range, we find the range of ϕ: $\phi_0 - \delta\phi \leqslant \phi \leqslant \phi_0 + \delta\phi$ by solving $\hat{n}\cdot\hat{b} = \cos 1/\gamma$. Note that the expression obtained for $\delta\phi$ is the same as that given in Gangadhara (2010) except for the fact that the angle τ has to be replaced with the one that we have given above. We note that the behavior of the beaming regions with respect to rotation phase ϕ' is mostly similar to the case of the unperturbed dipole of the non-rotating magnetosphere (Gangadhara 2010). Note that the whole beaming regions of the perturbed dipole get shifted in the coordinate ϕ with respect to those of the unperturbed dipole (see Figure 2).

3. POLARIZATION STATE OF THE RADIATION FIELD

The spectral distribution of the radiation field emitted by accelerating relativistic plasma at the observation point Q is given by (Jackson 1998)

$$\mathbf{E}(\mathbf{r},\omega) = \frac{1}{\sqrt{2\pi}}\frac{q e^{i\omega R_0/c}}{R_0 c} \times \int_{-\infty}^{+\infty} \frac{|\mathbf{b}|}{\kappa c}\frac{\hat{n}\times[(\hat{n}-\boldsymbol{\beta})\times\dot{\boldsymbol{\beta}}]}{\xi^2} e^{i\omega(t-\hat{n}\cdot\mathbf{r}/c)} d\theta. \quad (21)$$

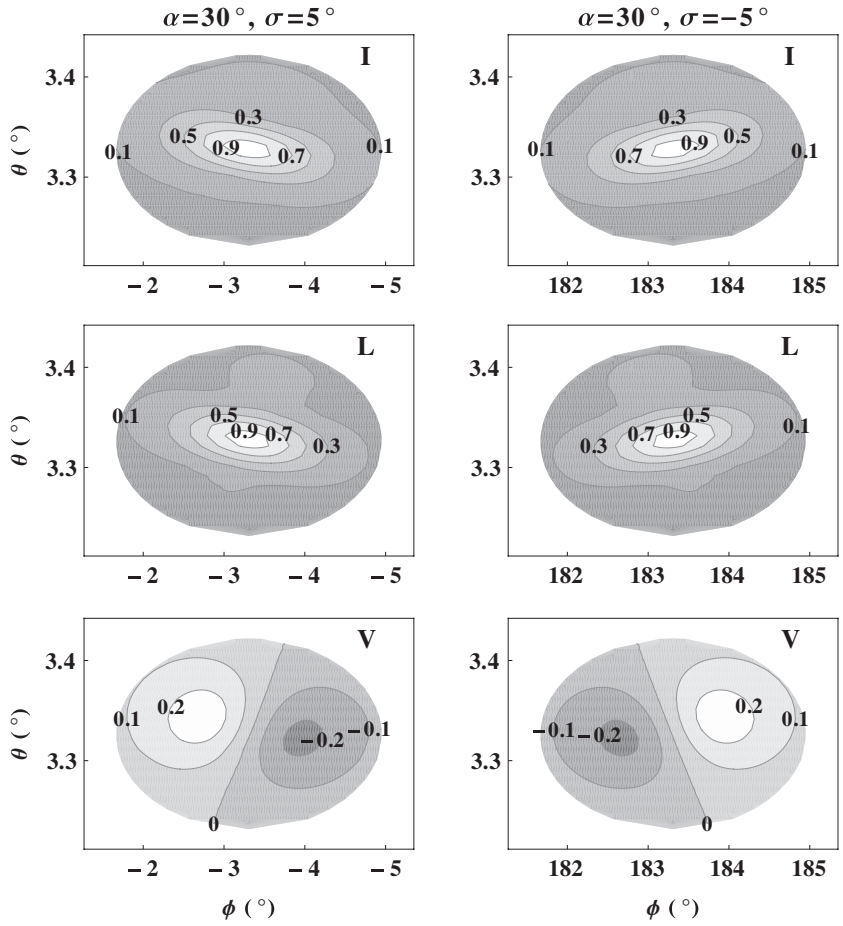

Figure 3. Polarization state of emissions from the beaming regions with uniform radiation source density at rotation phase $\phi' = 0°$. For simulation we have used the parameters $\alpha = 30°$, $\sigma = \pm 5°$, $r_n = 0.1$, $P = 1$ s, $\varsigma = 1$, $\gamma = 400$, and $\nu = 600$ MHz.

Note that the time t in the above equation has to be replaced by the expression given in Equation (6) of Kumar & Gangadhara (2012). Following the method given in Kumar & Gangadhara (2012), we solve the integral of Equation (21) and estimate the polarization state of the radiation field in terms of the Stokes parameters I, Q, U, and V, which are defined in Gangadhara (2010).

3.1. Emission with Uniform Radiation Source Density

By assuming a uniform radiation source distribution in the emission region of the magnetosphere, we estimated the polarization state of the emitted radiation. The simulated contour plots of total intensity I, linear polarization $L = \sqrt{Q^2 + U^2}$, and circular polarization V in the perturbed dipole configuration are given in Figure 3. The parameters used for simulation are $\alpha = 30°$, $\sigma = \pm 5°$, $r_n = 0.1$, $P = 1$ s, $\varsigma = 1$, $\gamma = 400$, $\nu = 600$ MHz, and the rotation phase is $\phi' = 0°$. Note that the parameters in each panel are normalized with the corresponding peak value of the total intensity. Also note that the contour plots are plotted in such a way that the emissions go from the leading side to the trailing side of the beaming regions in azimuth ϕ. The polarized emissions from the beaming region get rotated as indicated by the contour patterns in the (θ, ϕ)-plane compared to those due to the unperturbed dipole (see Figure 3 of Kumar & Gangadhara 2012). The rotation of the contour patterns is due to the perturbation of the actual dipole geometry by the PC-currents. Also it introduces an asymmetry into the beaming region emissions in such a way that there is a selective enhancement of emissions over the larger θ and larger ϕ regions due to a larger resultant curvature. This is very clear from the V parameter contour plots where there is a selective enhancement of the positive circular over the negative circular. Note that the direction of the rotation of contour patterns in the (θ, ϕ)-plane is opposite between the positive and negative σ cases. It is in the opposite direction to the one with a rotating dipole for positive σ while for negative σ it is in the same direction (see Kumar & Gangadhara 2012). Also note that the magnitude of the rotation of intensity patterns is found to be independent of the rotation phase of the magnetic axis unlike the other one due to the effect of the pulsar rotation where it noticeably decreases at outer phases.

The net emission that the observer receives at any instant of time will be an incoherent superposition of emissions from different plasma particles/bunches. Following Gangadhara (2010), we have simulated the polarization profiles: total intensity I_s, linear polarization L_s, circular polarization V_s, and polarization position angle $\psi_s = (1/2)\tan^{-1}(U_s/Q_s)$, and plotted them in Figure 4. For simulation, we used the same parameters as in Figure 3 and assumed that the source distribution is uniform throughout the emission region. The emission on the leading side ($\phi' < 0°$) is roughly the same as that on the trailing side ($\phi' > 0°$) due to the symmetry of the curvature of field lines on both the sides (see Figure 2), which is the same as in the unperturbed dipole geometry. Even though emissions from individual sources are highly polarized, the net emission from the

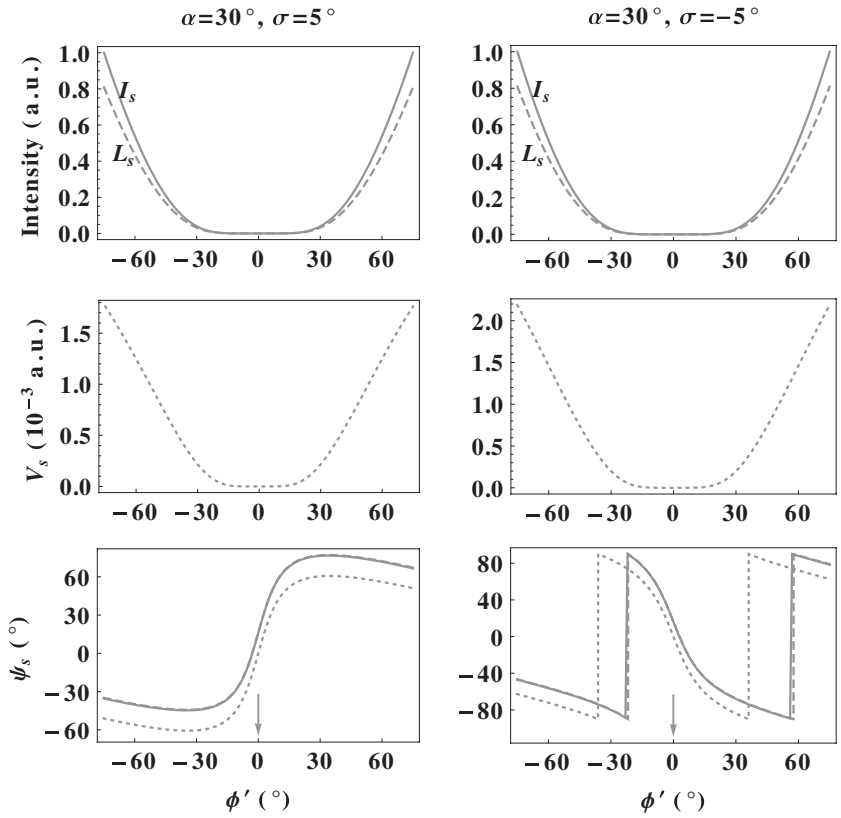

Figure 4. Simulated polarization profiles for emission with uniform source distribution. In the PPA (ψ_s) panels, dotted line curves represent the RVM for the unperturbed dipole, whereas dashed and solid ones represent the PPA in the perturbed dipole geometry derived from Hibschman & Arons (2001) and our calculations, respectively. The solid arrows point to the PPA inflection points from our simulation. The parameters chosen for simulation are the same as in Figure 3.

whole beaming region becomes less polarized due to the incoherent addition. However, a small quantity of positive circular polarization survives due to the asymmetry in the magnitudes of positive and negative polarities (see Figure 3), which becomes more significant when the source distribution becomes nonuniform. The PPA curves (solid line curves) shift upward with respect to those due to the unperturbed RVM model (dotted line curves) only, but the PPA inflection point is left mostly unchanged. For comparison, PPAs derived by Hibschman & Arons (2001) are also superposed with our simulations and both are in good agreement (see the dashed line curves). Note that Hibschman & Arons (2001) considered the emission from the beaming region center only, and the simulations show that the contributions from the neighboring emission points will have the least effect on the net PPA. However, they become important once there is a density gradient in the plasma distribution as we show later.

3.2. Radiation Emission from the Nonuniform Distribution of Sources

The sub-pulses in the pulsar individual pulses suggest that the emission region of the pulsar magnetosphere may not be filled with a uniform plasma density. When the observer's sight line encounters plasma columns, which are associated with the sparks activity on the polar cap, components such as features in intensity can result. Hence the net emission that the observer receives will be modulated emission over the uniform background emission. We model the nonuniform source distribution in the emission region in terms of the "modulation" function as considered in Kumar & Gangadhara (2012). The intensity components of average profiles are assumed to be nearly Gaussian in shape, and hence they have been fitted with an appropriate Gaussian (e.g., Kramer et al. 1994). We define the modulation function as

$$f(\theta, \phi) = f_0 f_\theta f_\phi, \tag{22}$$

where f_0 is the amplitude, and $f_\theta = \exp[-(\theta - \theta_p)^2/\sigma_\theta^2]$ and $f_\phi = \exp[-(\phi-\phi_p)^2/\sigma_\phi^2]$ are the Gaussian modulations in θ and ϕ, respectively. The parameters (θ_p, ϕ_p) define the peak location of the Gaussian and $\sigma_\theta = w_\theta/(2\sqrt{\ln 2})$ and $\sigma_\phi = w_\phi/(2\sqrt{\ln 2})$, where w_θ and w_ϕ are the corresponding FWHM of the Gaussian in the two directions.

3.2.1. Emission with Azimuthal Modulation

By considering a modulation in the magnetic azimuthal direction that has a peak location in the magnetic meridional plane in two cases ($\phi_p = 0^\circ$ for $\sigma = 5^\circ$ and $\phi_p = 180^\circ$ for $\sigma = -5^\circ$), we computed the polarization profiles and show them in Figures 5 and 6, respectively. For the simulation we used the parameters $f_0 = 1$, $f_\theta = 1$, and other parameters that are the same as in Figure 3. In the case of $\sigma = 5^\circ$ (see Figure 5), the intensity peak shifted to a later phase whereas for $\sigma = -5^\circ$ it gets shifted to an earlier phase (see Figure 6). Due to the perturbation of the magnetic field, the emission locations are shifted in the magnetic azimuth as shown in Figure 2, and hence, the intensity gets phase shifted to the later and earlier phases for the positive and negative σ sight lines, respectively. The phase shifts of the intensity peaks in the case of $\sigma = 5^\circ$, $\sigma_\phi = 0.1$ and 0.4 are found to be $0\overset{\circ}{.}54$ and $7\overset{\circ}{.}22$, respectively, whereas those in the case of $\sigma = -5^\circ$, $\sigma_\phi = 0.1$ and 0.25 are found to be $-0\overset{\circ}{.}75$ and $-1\overset{\circ}{.}50$, respectively. The increase in the phase shift

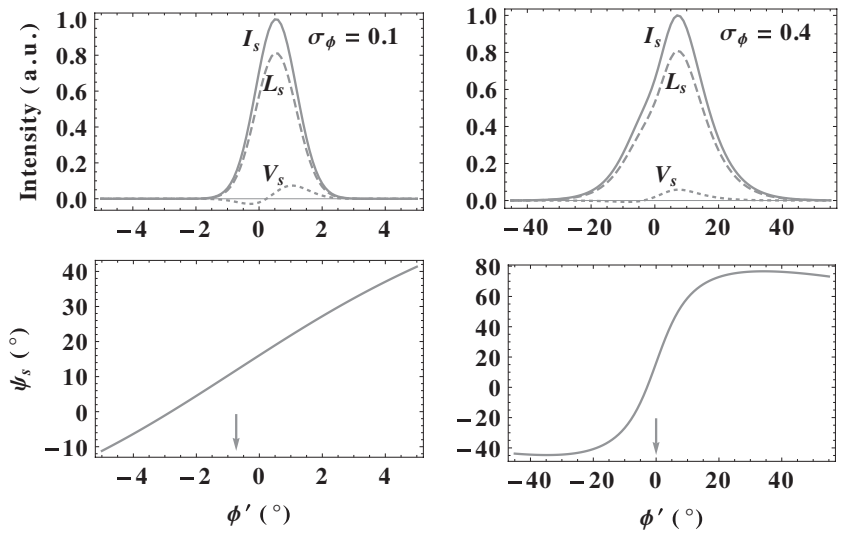

Figure 5. Simulated polarization profiles for emission from the nonuniform distribution of sources (modulation) in the azimuthal direction for the $\sigma = 5^\circ$ case. The parameters used for simulation are $f_0 = 1$, $f_\theta = 1$, $\phi_p = 0^\circ$, and the other parameters are the same as in Figure 3.

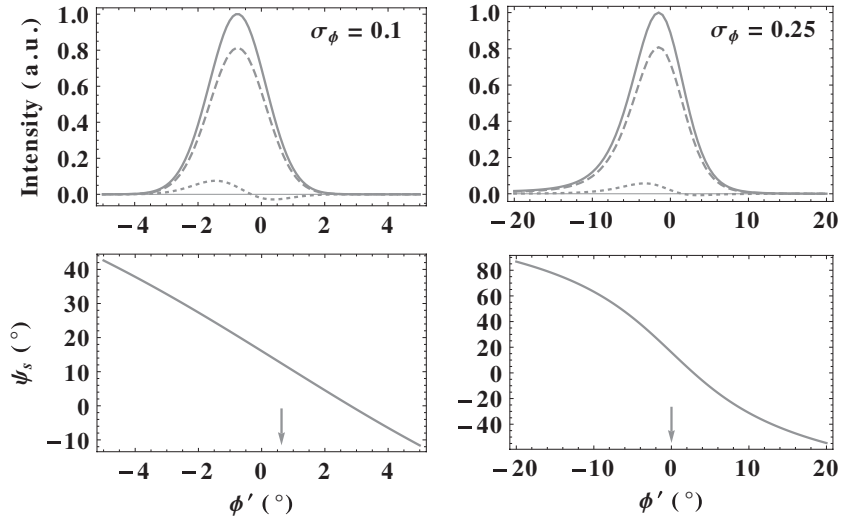

Figure 6. Same as Figure 5 except $\sigma = -5^\circ$ and $\phi_p = 180^\circ$.

of the intensity peaks with increasing σ_ϕ can be explained as follows. In the perturbed dipole geometry, the emission locations (particularly in the magnetic azimuth) get phase shifted with respect to the unperturbed one. Because of this phase shift, the curvature of the source trajectory becomes asymmetric about the antisymmetric point of the magnetic azimuth. For $\sigma = 5^\circ$ the curvature becomes larger on the trailing side of $\phi_p = 0^\circ$ compared to that on the leading side, whereas it is the opposite about $\phi_p = 180^\circ$ for $\sigma = -5^\circ$ (see Figure 2). Therefore, the phase shift of the modulated intensity peaks will be larger than ϕ_p (where the modulation peak is located), and this extra phase shift becomes larger for the broader modulation. Furthermore, the intensity component gets broader as well as shifted farther in the negative σ as the modulation is mapped onto the broader region in the observer's frame compared to that in the positive σ (see the case of $\sigma_\phi = 0.1$ in Figures 5 and 6).

Circular polarization V_s is antisymmetric for the steeper modulation ($\sigma_\phi = 0.1$), and changes sign from negative to positive in the case of $\sigma = 5^\circ$ and from positive to negative in the case of $\sigma = -5^\circ$. In both cases ($\sigma = \pm 5^\circ$), the positive circular becomes stronger compared to the negative circular due to an enhancement of the unmodulated positive circular over the negative circular (see Figure 3). Also the phase location of the sign reversal of the circular either leads or lags the intensity peak due to the above said asymmetry. In the case of broader modulation ($\sigma_\phi = 0.4$ and 0.25), the circular becomes almost positive throughout the pulse. Hence it becomes almost symmetric as the effect of the modulation becomes less significant over the beaming regions in comparison with the induced asymmetry between the unmodulated positive and negative circulars that resulted from the PC-currents.

Linear polarization L_s almost follows the total intensity I_s profile with a lower magnitude due to an incoherent addition of emissions within the beaming region. Further, it is slightly enhanced on the leading side where the circular is smaller than on the trailing side in the case of $\sigma = 5^\circ$, and vice versa in the case of $\sigma = -5^\circ$. PPA is increasing ("counterclockwise" or "ccw" swing as $d\psi_s/d\phi' > 0$) in the case of $\sigma = 5^\circ$, while decreasing ("clockwise" or "cw" swing as $d\psi_s/d\phi' < 0$) for $\sigma = -5^\circ$. Hence, in the case of pulsars with antisymmetric-type circular polarization we find the correlation of the sense reversal of circular polarization from negative to positive with

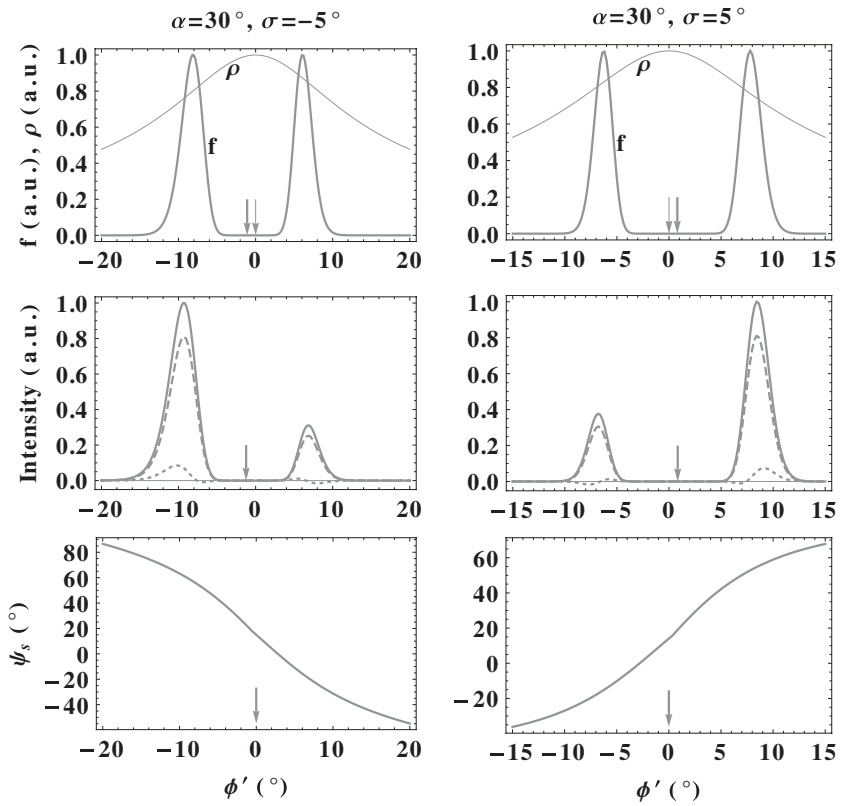

Figure 7. Same as Figure 5 except $\phi_p = 180^\circ \pm 30^\circ$ for $\sigma = -5^\circ$, and $\phi_p = \pm 40^\circ$ for $\sigma = 5^\circ$. In the top row panels, the thick line curve represents the modulation strength f whereas the thin line curve represents the corresponding radius of curvature ρ; the thick line arrows mark the midpoint of the modulation peaks whereas the thin line arrows mark the symmetric point of ρ. Both f and ρ are normalized with their corresponding maximum values.

the increasing PPA and vice versa. The inflection point of PPA is mostly unaffected for the broader modulation, similar to the one with an unmodulated emission (see Figure 4). But for a steeper modulation ($\sigma_\phi = 0.1$), it is shifted to the earlier phase in the case of $\sigma = 5^\circ$ and to the later phase in the case of $\sigma = -5^\circ$, which is opposite of the intensity phase shifts. Note that the phase shift of the PPA inflection is found to be shifted toward the stronger L_s side. The phase shifts of the PPA inflection point in the cases of $\sigma = \pm 5^\circ$ with $\sigma_\phi = 0.1$ are found to be $0\overset{\circ}{.}73$ and $0\overset{\circ}{.}63$, respectively. The smaller phase shift of the PPA inflection point in the case of $\sigma = -5^\circ$, as compared to that in the case of $\sigma = 5^\circ$, is due to effective broadening of the modulation in the observer's frame.

For the next case we consider the modulation symmetrically located on either side with respect to the meridional plane: $\phi_p = 180^\circ \pm 30^\circ$ for $\sigma = -5^\circ$ and $\phi_p = \pm 40^\circ$ for $\sigma = 5^\circ$. The simulated polarization profiles are shown in Figure 7. The modulation strength f that the observer finds at the beaming region center and the corresponding radius of curvature ρ of the particle's trajectory are also given. Even though ρ is roughly symmetric at about $\phi' = 0$, it becomes asymmetric in strength at the modulation peaks between the leading and trailing sides. The ρ at the modulation peak on the leading side becomes smaller than that on the trailing side in the case of $\sigma = -5^\circ$, and vice versa in the case of $\sigma = 5^\circ$. This is due to the phase shift of the modulation peaks (the mid point of the modulation peaks is indicated by the thick arrows) from the phase shift of the emission points (see Figure 2). As a result, an asymmetry arises in the strength of the intensity components between the leading and trailing sides: the component on the leading side becomes stronger than that on the trailing side in the case of $\sigma = -5^\circ$ and vice versa in the case of $\sigma = 5^\circ$. Also, since ρ at the modulation peak on the leading side becomes less steep than that on the trailing side in the case of $\sigma = -5^\circ$, the leading component becomes broader and vice versa in the case of $\sigma = 5^\circ$ as indicated by the second row panels. In both the cases of σ, similar to the modulation, the outer phase emissions become stronger than the inner ones, and V_s clearly shows that. However the larger asymmetry between the positive and negative circulars under the leading side component in the $\sigma = -5^\circ$ case and that under the trailing one in the $\sigma = 5^\circ$ case is due to the selective enhancement of the positive circular of the unmodulated emissions (see Figure 3).

3.2.2. Emission with Polar Modulation

By assuming a hollow cone modulation around the magnetic axis, i.e., a plasma density gradient only in the polar direction, we simulated the polarization profiles, which are shown in Figures 8 and 9. The parameters used for the simulation are $f_0 = 1$, $f_\phi = 1$, and the rest are the same as in Figure 3. In the cases of $\theta_p = 3^\circ$ and $\sigma_\theta = 0.005$ and 0.002, since the minimum of $\theta \sim (2/3)\sigma = 3\overset{\circ}{.}3$, the observer sight line just grazes the hollow emission cone and hence a single intensity component is observed. But in the case of $\theta_p = 4^\circ$ and $\sigma_\theta = 0.003$ the observer sight line cuts the hollow cone twice and hence results in double components. In all cases, the intensity peak (the I_s peak in the cases of $\theta_p = 3^\circ$ and $\sigma_\theta = 0.005$, and 0.002 and the mid point of the intensity peaks in the case of $\theta_p = 4^\circ$ and $\sigma_\theta = 0.003$) more or less remains at $\phi' = 0^\circ$. This is because, even with the perturbation of the dipole, both the colatitude and the corresponding radius of the curvature remain symmetric about $\phi' = 0^\circ$. However, there is a small phase shift of the PPA

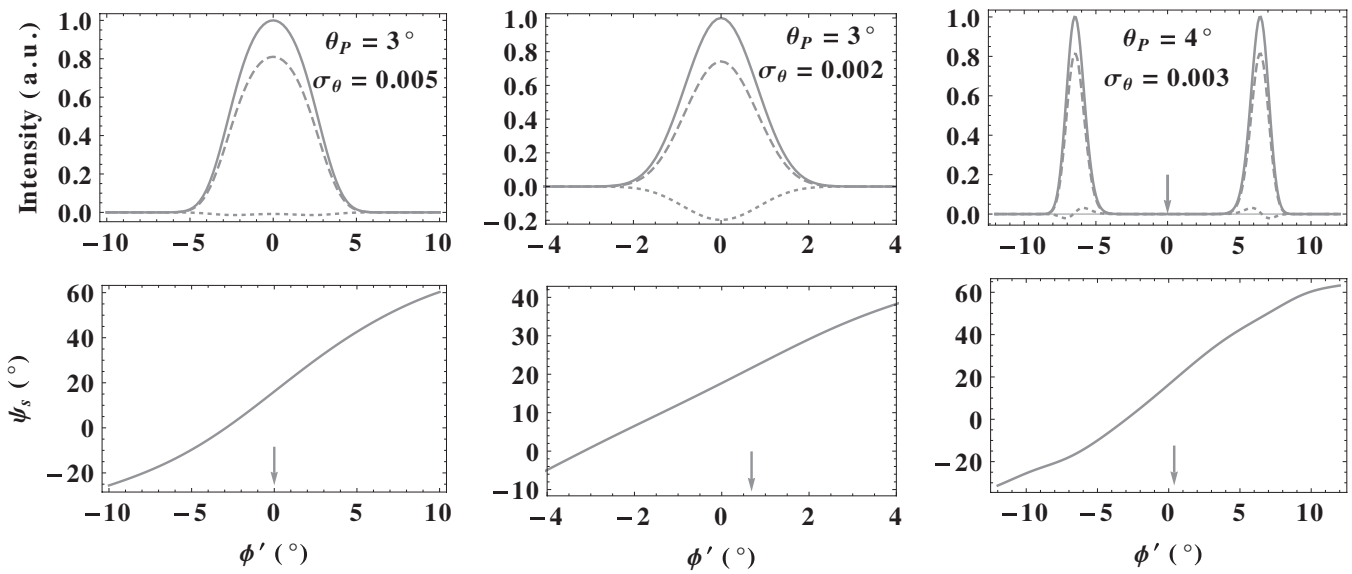

Figure 8. Simulated polarization profiles for emission with a modulation in the polar direction for the case of $\sigma = 5°$. Here $f_0 = 1$, $f_\phi = 1$, and the other parameters are the same as in Figure 3.

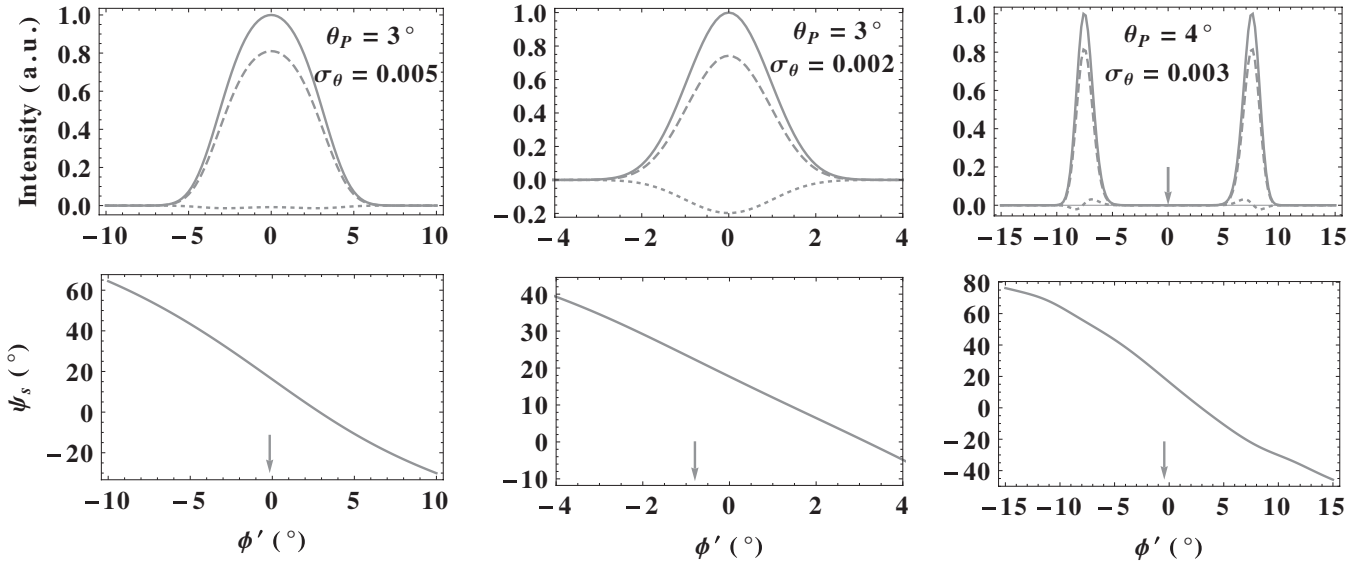

Figure 9. Same as Figure 8 except for $\sigma = -5°$ and $\phi_p = 180°$.

inflection point in the cases of $\theta_p = 3°$ and $\sigma_\theta = 0.002$, and $\theta_p = 4°$ and $\sigma_\theta = 0.003$, but the shift is in the opposite direction between the $\sigma = \pm 5°$ cases.

In the case of $\theta_p = 3°$ and $\sigma_\theta = 0.005$, a tiny circular survives due to a less steep modulation, but in the cases of $\theta_p = 3°$ and $\sigma_\theta = 0.002$, and $\theta_p = 4°$ and $\sigma_\theta = 0.003$ it is quite significant. In the case of $\theta_p = 3°$ and $\sigma_\theta = 0.002$ where the observer sight line grazes the modulation at a larger colatitude, a symmetric-type negative circular is observed due to the selective enhancement of beaming region emissions over the smaller θ part (see Figure 3). But in the case of $\theta_p = 4°$ and $\sigma_\theta = 0.003$, an antisymmetric-type circular is observed with the sign changing from negative to positive under the leading component and vice versa on trailing. This is due to the selective enhancement of emissions over either smaller values of θ or larger depending upon when the sight line crosses the hollow cone. Note that with the modulation in θ, the sign reversal of the circular is the same for both cases of σ unlike the case with modulation in ϕ (see Figures 5 and 6). Since the beaming region emission, due to the uniform source distribution, has a larger positive circular than the negative circular (see Figure 3), modulated profiles also show a slightly larger positive circular than the negative circular.

3.2.3. Emission with Modulation in both the Magnetic Colatitude and Azimuth

In general, the plasma distribution can be nonuniform in both the polar and azimuthal directions and hence we consider the modulation in both θ and ϕ. The extreme cases of modulation, modulation in ϕ dominating over that in θ for $\sigma_\phi \ll \sigma_\theta$ and the modulation in θ dominating over that in ϕ for $\sigma_\theta \ll \sigma_\phi$, are detailed in Sections 3.2.1 and 3.2.2, respectively. The simulations with the combinations of modulation parameters used in Sections 3.2.1 and 3.2.2 give the general polarization profiles.

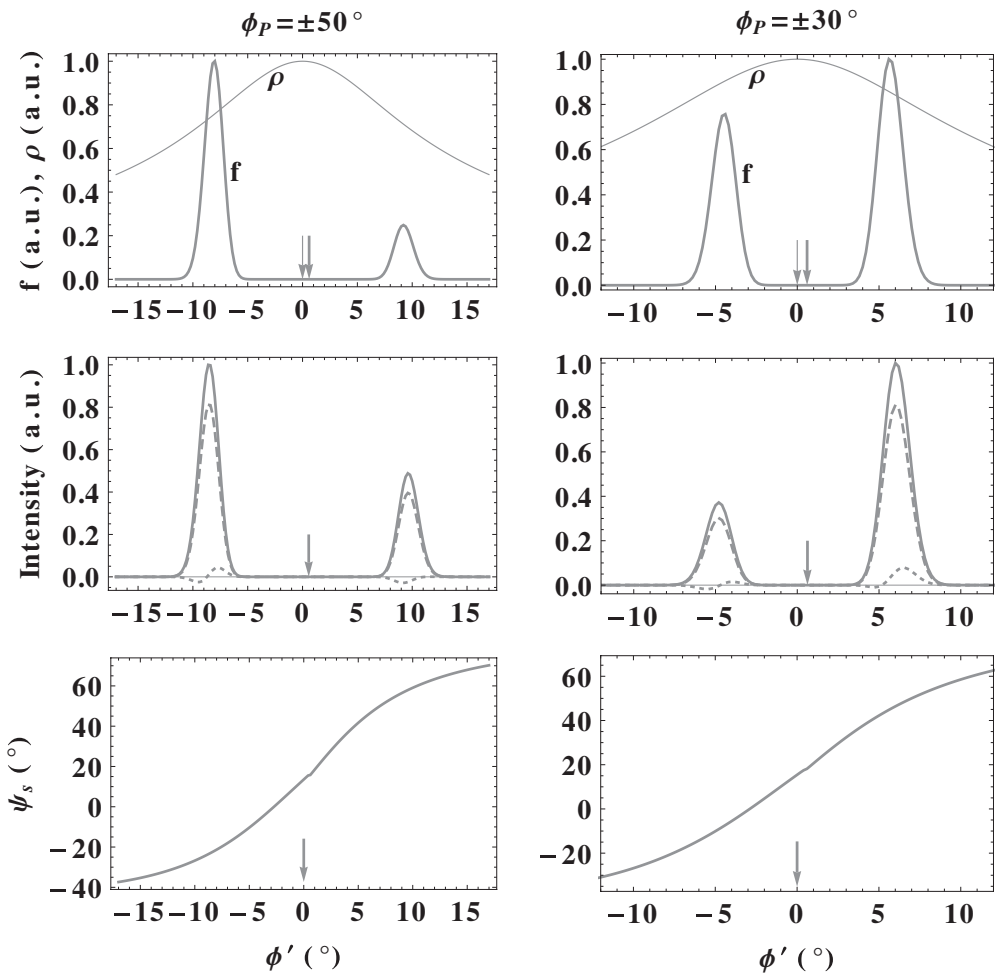

Figure 10. Simulated polarization profiles for emission with a modulation in both the polar and azimuthal directions for the case of $\sigma = 5^\circ$. Here $f_0 = 1$, $\theta_p = 4^\circ$, $\sigma_\theta = 0.01$, $\sigma_\phi = 0.1$, and the other parameters are the same as in Figure 3.

For the case with the Gaussian modulation, with peaks located symmetrically on either sides of the magnetic meridional plane in the conal ring of colatitude 4°, we consider two sets of azimuthal peak locations at $\phi_p = \pm 50^\circ$ and $\pm 30^\circ$. The simulated polarization profiles are given in Figure 10 for the case of $\sigma = 5^\circ$. For simulation, we used $f_0 = 1$, $\sigma_\theta = 0.01$, $\sigma_\phi = 0.1$, and the other parameters are the same as in Figure 3. Since the phase shift of the emission points from the PC-current is only in ϕ and not in θ, the observer sight line selectively encounters the modulation depending upon their azimuthal locations as shown in Figure 10. The sight line encounters a stronger modulation on the leading side as it passes closer to the Gaussian peak than that on the trailing side in the case $\phi_p = \pm 50^\circ$, and vice versa in the case $\phi_p = \pm 30^\circ$. However, the asymmetry in the strength of the components between the leading and trailing sides becomes enhanced or reduced in the intensity profiles depending upon the asymmetry in the curvature at the modulation peaks as explained earlier for Figure 7. The ρ at the modulation peak on the leading side becomes larger than that on the trailing side. Hence there is a decrease in the asymmetry in the strengths of the modulated intensity components between the leading and trailing sides in the case of $\phi_p = \pm 50^\circ$, whereas it increases in the case of $\phi_p = \pm 30^\circ$. The inner circulars become stronger than the outer ones in the case of $\phi_p = \pm 50^\circ$ as the observer selectively encounters the modulated regions that are closer to the magnetic meridional plane, and vice versa in the case of $\phi_p = \pm 30^\circ$. Further, it is more pronounced on the trailing side than that on the leading side due to an asymmetry in the modulation encountered by the observer.

Note that if one considers the modulation in the θ direction, which is even steeper, then the circular becomes an almost symmetric type with the sign of inner circulars for $\phi_p = \pm 50^\circ$, and only the outer circulars sign for $\phi_p = \pm 30^\circ$. Also note that if one chooses a negative sight line $\sigma = -5^\circ$ and the modulation peaks are situated symmetrically in the azimuthal direction with respect to the meridional plane, then the behavior of the strength of the modulation that the sight line encounters and intensity components on the leading and trailing sides will be opposite to the case of $\sigma = 5^\circ$.

3.3. Emission from the Southern Hemisphere

So far we have considered the emissions from the northern hemisphere of the pulsar magnetosphere, which lies toward the positive $\mathbf{\Omega}$. However, one can receive emissions from the southern hemisphere that lies toward the negative $\mathbf{\Omega}$. By considering $\alpha = 180^\circ$–30° and the azimuthal nonuniform source distribution, we have simulated the polarization profiles for the emission from the southern hemisphere for the two cases of $\zeta = 180^\circ$–35° and 180°–25°. The simulated profiles are given in Figure 11. The simulations show that the emission from the southern hemisphere for the case of $\zeta = 180^\circ$–35° is similar to the case of $\sigma_\phi = 0.1$ of Figure 5, except with the opposite sign

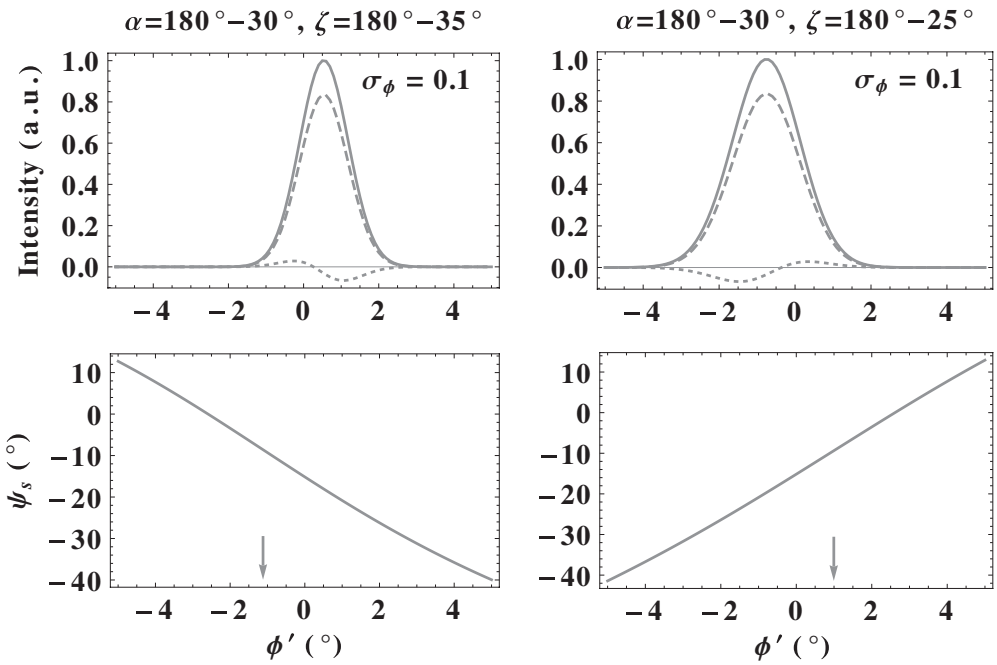

Figure 11. Simulated polarization profiles for emission from the southern hemisphere for the cases of $\alpha = 180°$–$30°$, and $\zeta = 180°$–$35°$ and $180°$–$25°$. Here the other parameters used for simulation are the same as in Figures 5 and 6 except $\sigma = -5°$ and $\phi_p = 180°$ for the $\zeta = 180°$–$35°$ case, and $\sigma = 5°$ and $\phi_p = 0°$ for the $\zeta = 180°$–$25°$ case.

for circular polarization and opposite PPA swing. Similarly, the emission in the case $\zeta = 180°$–$25°$ is similar to that in the case $\sigma_\phi = 0.1$ of Figure 6. Note that this behavior remains the same even with the nonuniform source distribution in both the polar and azimuthal directions that we have considered in the case of Figure 10.

4. DISCUSSION

The PC-current-perturbed dipole field is axisymmetric with respect to the magnetic axis wherein the field lines are twisted around the magnetic axis due to an azimuthal component. Since the plasma particles (or bunches) are constrained to move along the field lines, the beaming direction of the relativistic emission gets aberrated toward the direction of a tangent of twisted field lines. As a result, for the case of the positive σ sight line, the emission points of the perturbed dipole field are shifted to later phases (or later times) in the magnetic azimuth than those of the unperturbed dipole field, and vice versa for the case of the negative σ sight line. Since the induced twist of field lines is around the magnetic axis only, the emission points are found to be more or less unaffected in the magnetic colatitude. As the perturbed dipole field remains axisymmetric, for a given field line constant r_e, the radius of the curvature of the perturbed dipole field lines becomes a function of colatitude only. Hence the curvature remains symmetric about $\phi' = 0$, which is similar to the magnetic colatitude. Therefore the emission due to the uniform radiation source distribution and its polarization profiles remain symmetric about $\phi' = 0$ as shown in Figure 4, which is similar to the emission in the unperturbed dipole field, except for the survival of a small circular polarization due to a PC-current-induced asymmetry.

However, due to the nonuniform source distribution with a density gradient effectively in the magnetic azimuth, the modulated intensity components get shifted in each phase. Since the phase shift of the magnetic azimuth between the two cases ($\pm\sigma$) is of opposite directions, the modulated intensity components shift to the later phase in the case of positive σ and to the earlier phase in the case of negative σ. Even though the radius of curvature ρ is symmetric about $\phi' = 0$, it becomes asymmetric about the shifted modulation peak where the observer encounters the maximum plasma density. Hence, the phase shift of modulated intensity components becomes significantly different from that of the peak location of the broader modulation. But the intensity components do not get shifted in phase if the modulation is effective only in the polar direction as both θ and ρ remain symmetric about $\phi' = 0$.

Hibschman & Arons (2001) have shown that due to the distortion of the underlying dipole field, the resultant PPA curve gets an upward shift in the PPA versus rotation phase diagram, but the inflection point remains roughly unchanged. Our simulations do confirm the results of Hibschman & Arons (2001) in the case of unmodulated emission. However, once the radiation source distribution becomes nonuniform with a larger density gradient, as we showed in Sections 3.2, the phase shift of the PPA inflection point becomes quite significant. Note that, if there are phase shifts between the intensity components and that of the PPA inflection point then they will be in opposite directions.

Since the phase shift of emission points in the perturbed dipole field occurs only in the magnetic azimuth but not in the colatitude, the observer in general encounters an asymmetry in the strength of the two directional (polar and azimuthal) modulations between the leading and trailing sides as shown in Figure 10. Depending upon the azimuthal peak location of the Gaussian modulation in a given cone, the sight line selectively encounters the modulation either on the leading side or the trailing side. Hence, an asymmetry arises in the strength of the intensity components between the leading and trailing sides. However, the asymmetry in the intensity profiles could get enhanced or reduced. This depends upon the asymmetry in the curvature of the source trajectory at the modulation peaks

between the two sides, which is induced due to the phase shift of the modulation peaks. Note that, even with modulation only in the azimuthal direction, an asymmetry arises in the strength of the intensity components between the leading and trailing sides as shown in Figure 7.

We showed that both the "antisymmetric" (with an asymmetry in the strength between the opposite circular polarization polarities, in general) and "symmetric" types of circular polarization could be observed anywhere within the pulse window. This is possible due to an induced asymmetry in the polarized emission from the beaming region, such as the asymmetry between the positive and negative polarities, and asymmetry due to the rotation of circular contour patterns in the (θ, ϕ)-plane, the modulation of emission due to the nonuniform distribution of sources.

Our simulations show that the sign reversal of circular polarization near the central region of the pulse profile from negative to positive is correlated with the increasing PPA (wherein the PPA curve has a positive slope) and vice versa. This behavior is found in many pulsars (Radhakrishnan & Rankin 1990) and has been confirmed by Gangadhara (2010) and Kumar & Gangadhara (2012). However, there is also an association of the sign reversal of the circular polarization from positive to negative with the increasing PPA and vice versa (Han et al. 1998; You & Han 2006). In the case of pulsars with the sign reversal of circular polarization not associated with the central core region, You & Han (2006) have found that both the sign reversals of the circular from negative to positive and from positive to negative are associated with both the increasing and the decreasing PPA, and our simulation of double component pulse profiles confirms this behavior. In pulsars with the symmetric type of circular polarization, we observed no correlation between the sense of circular polarization and the PPA swing. Hence we confirm the findings of Han et al. (1998) that the positive circular could be associated with either the increasing or decreasing PPA, and similarly, the negative circular too. Note that Kumar & Gangadhara (2012) have also confirmed these findings in the emissions from the rotating dipole.

The $\boldsymbol{E} \times \boldsymbol{B}$ drift on the spark-associated plasma filaments makes them rotate around the magnetic axis, and serves as a natural and physical mechanism for the sub-pulse drift phenomenon (Ruderman & Sutherland 1975). The effects of the $\boldsymbol{E} \times \boldsymbol{B}$ drift and the PC-current are similar, in the sense that both of them introduce an azimuthal component of velocity to the plasma in addition to the velocity in the direction of tangents to the dipolar field lines. The aberration angle η' (Gangadhara 2005) between the unperturbed velocity $\boldsymbol{v_0}$ and the perturbed velocity $\boldsymbol{v}$, given by $\cos\eta' = \hat{v}_0 \cdot \hat{v}$, where $\hat{v}_0 = \boldsymbol{v_0}/|\boldsymbol{v_0}|$ and $\hat{v} = \boldsymbol{v}/|\boldsymbol{v}|$, can be used to investigate the significance of one over the other. For the case of the $\boldsymbol{E} \times \boldsymbol{B}$ drift, the perturbed velocity is given by $\boldsymbol{v} = \boldsymbol{v_0} + \boldsymbol{v_1}$, where $\boldsymbol{v_1} = 2\pi(\partial \boldsymbol{r}/\partial\phi)/\hat{p}_3$ is the drift velocity around the magnetic axis with $\hat{p}_3$ being the time taken by the plasma filament to complete one full rotation around the magnetic axis. By considering observationally quoted values for $\hat{p}_3$ in the literature (see Gil et al. 2003 and references therein), we find the ratio of η' due to $\boldsymbol{E} \times \boldsymbol{B}$ to that due to the PC-current. It is ~3%–4% for slow drifting pulsars (e.g., it is about 3% for PSR B0943+10 and 4% for PSR B2319+60 whose $\hat{p}_3 \sim 37P$ and $\sim 70P$, respectively) and ~8%–15% for fast drifting pulsars (e.g., it is about 8% for PSR B2303+30 and 15% for PSR B0826−34 whose $\hat{p}_3 \sim 23P$ and $\sim 14P$, respectively). Therefore, we believe that the PC-currents are more significant in comparison with the $\boldsymbol{E} \times \boldsymbol{B}$ drift in influencing the emission beam geometry and polarization, unless the pulsar drifting is very fast (i.e., $\hat{p}_3 \sim P$).

In this work, we considered the altitude-independent PC-current density, but in reality it could have an altitude dependency due to the diverging nature of the dipolar field lines and conservation of escaping plasma. Since we considered constant emission altitude r across the pulse profile, our simulations are still valid in explaining the trend of the effect of the PC-current on pulsar polarization profiles. However, if one considers the emissions from a range of altitude that increases from inner to outer phases (e.g., Gangadhara & Gupta 2001; Gupta & Gangadhara 2003; Dyks et al. 2004), then the altitude-dependent current density would be more appropriate. Our aim was to understand the role of the PC-current on pulsar radio emission and polarization, and we did not consider the pulsar rotation here. However, the combined role of PC-currents and the rotation on the pulsar radio emission and polarization needs to be investigated.

5. CONCLUSION

By considering the PC-current-induced perturbation on the dipole field we have developed a model for the pulsar radio emission and polarization. By incorporating the nonuniform distribution of radiation sources in the emission region of the distorted dipole field, we have simulated a few typical polarization pulse profiles. Based on our simulations, we conclude the following points.

1. Due to the PC-current-induced perturbation of the underlying dipole field, the emission points in the magnetic azimuth get shifted to later phases in the case of positive σ, and to earlier phases in the case of negative σ compared to those due to unperturbed ones (see Figure 2).
2. The intensity components that resulted from the modulation that dominated in the azimuthal direction over that in the polar direction shift to either later or earlier phases depending upon the viewing geometry. The magnitude of the phase shift depends upon the steepness of the modulation and the PC-current-induced asymmetry in the curvature of the source trajectory.
3. Due to the PC-current-induced asymmetry and modulation, there arises a small phase shift in the PPA inflection point, too.
4. The leading side intensity components could become stronger and broader than the corresponding trailing ones or vice versa depending upon the viewing geometry and azimuthal location of the Gaussian modulation peaks in the concentric cones.
5. Both the "antisymmetric"-type circular polarization with usual asymmetry in the strength of the opposite polarities and the "symmetric"-type circular polarization become possible anywhere within the pulse window. It depends upon the viewing geometry and modulation in the emission region of the perturbed dipole field.

We thank the anonymous referee for useful comments.

REFERENCES

Barnard, J. J., & Arons, J. 1986, ApJ, 302, 138
Blaskiewicz, M., Cordes, J. M., & Wasserman, I. 1991, ApJ, 370, 643
Cheng, A. F., & Ruderman, M. A. 1979, ApJ, 229, 348
Cheng, A. F., & Ruderman, M. A. 1980, ApJ, 235, 576

Dyks, J. 2008, MNRAS, 391, 859
Dyks, J., Rudak, B., & Harding, A. K. 2004, ApJ, 607, 939
Dyks, J., Wright, G. A. E., & Demorest, P. 2010, MNRAS, 405, 509
Gangadhara, R. T. 1997, A&A, 327, 155
Gangadhara, R. T. 2005, ApJ, 628, 923
Gangadhara, R. T. 2010, ApJ, 710, 29
Gangadhara, R. T., & Gupta, Y. 2001, ApJ, 555, 31
Gil, J., Melikidze, G. I., & Geppert, U. 2003, A&A, 407, 315
Gil, J. A., & Snakowski, J. K. 1990a, A&A, 234, 237
Gil, J. A., & Snakowski, J. K. 1990b, A&A, 234, 269
Goldreich, P., & Julian, W. H. 1969, ApJ, 157, 869
Gupta, Y., & Gangadhara, R. T. 2003, ApJ, 584, 418
Han, J. L., Manchester, R. N., Xu, R. X., & Qiao, G. J. 1998, MNRAS, 300, 373
Hibschman, J. A., & Arons, J. 2001, ApJ, 546, 382
Jackson, J. D. 1998, Classical Electrodynamics (New York: Wiley)
Kramer, M., Wielebinski, R., Jessner, A., Gil, J. A., & Seiradakis, J. H. 1994, A&AS, 107, 515
Kumar, D., & Gangadhara, R. T. 2012, ApJ, 746, 157
Lyne, A. G., & Manchester, R. N. 1988, MNRAS, 234, 477
McKinnon, M. M. 1997, ApJ, 475, 763
McKinnon, M. M., & Stinebring, D. R. 1998, ApJ, 502, 883
Melrose, D. B. 2003, in ASP Conf. Ser. 302, Radio Pulsars, ed. M. Bailes, D. J. Nice, & S. E. Thorsett (San Francisco, CA: ASP), 179
Michel, F. C. 1987, ApJ, 322, 822
Mitra, D., & Deshpande, A. A. 1999, A&A, 346, 906
Mitra, D., & Rankin, J. M. 2002, ApJ, 577, 322
Radhakrishnan, V., & Cooke, D. J. 1969, ApJ, 3, L225
Radhakrishnan, V., & Rankin, J. M. 1990, ApJ, 352, 258
Rankin, J. M. 1983, ApJ, 274, 333
Rankin, J. M. 1990, ApJ, 352, 247
Rankin, J. M. 1993, ApJS, 85, 145
Ruderman, M. A., & Sutherland, P. G. 1975, ApJ, 196, 51
Sturrock, P. A. 1971, ApJ, 164, 229
Thomas, R. M. C., & Gangadhara, R. T. 2007, A&A, 467, 911
Thomas, R. M. C., & Gangadhara, R. T. 2010, A&A, 515, 86
Thomas, R. M. C., Gupta, Y., & Gangadhara, R. T. 2010, MNRAS, 406, 1029
Xilouris, K. M., Kramer, M., Jessner, A., et al. 1998, ApJ, 501, 286
You, X. P., & Han, J. L. 2006, Chin. J. Astron. Astrophys., 6, 237